Deep–Sea Research I 230 (2026) 104704

Contents lists available at ScienceDirect

Deep-Sea Research Part I

journal homepage: www.elsevier.com/locate/dsri

# Spectral transformations of swell in ocean eddy dipoles from SAR observations and numerical simulations

Nelson Violante-Carvalho [a], Thiago de Paula [a,b], Leandro Calado [c], Luigi Cavaleri [d], Felipe Marques dos Santos [e],*, Luiz Mariano Carvalho [f], Andre Luiz Cordeiro dos Santos [g], Alvise Benetazzo [d]

[a] *Ocean Engineering Program, Rio de Janeiro Federal University (COPPE-UFRJ), Brazil*
[b] *Department of Oceanic Engineering Technology, Petrobras Research and Development Center (CENPES), Brazil*
[c] *Admiral Paulo Moreira Marine Studies Institute, Brazilian Navy (IEAPM), Brazil*
[d] *Istituto di Scienze Marine, Consiglio Nazionale delle Ricerche (CNR-ISMAR), Italy*
[e] *National Oceanography Centre, Southampton, UK*
[f] *Mathematics and Statistics Institute, Rio de Janeiro State University (UERJ), Brazil*
[g] *Mathematics Institute, Federal Center for Technological Education of Rio de Janeiro (CEFET-RJ), Brazil*

## ARTICLE INFO

*Keywords:*
SAR Synthetic Aperture Radar
Ocean eddy dipole
Wave–current interactions
Wave spectra
Hasselmann SAR-wave mapping relation

## ABSTRACT

Mesoscale eddies are energetic oceanic structures that contribute substantially to the ocean's kinetic energy. They frequently occur in pairs, known as eddy dipoles or mushroom-like eddies, and are potentially ubiquitous in the global ocean. These dipoles generate an intense surface current along their central axis, forming a narrow jet that is considerably stronger than the surrounding flow. We investigate the influence of the central jet of an eddy dipole on the properties and spectral shape of wind waves propagating in opposition to the current. To capture the complex modifications induced by wave–current interactions, a novel inversion method is applied to retrieve directional wave spectra from Synthetic Aperture Radar (SAR) data acquired along an Envisat ground track that crossed an eddy dipole on the Sao Paulo Plateau in the Southwestern Atlantic. The observational analysis is complemented by idealized numerical simulations using state-of-the-art wave and ocean circulation models. Furthermore, the positions and structures of the eddy dipoles and their associated jets are identified using absolute dynamic topography and derived absolute surface geostrophic velocities from satellite altimetry. The results demonstrate that, under favorable geometric conditions, eddy dipoles act as focal lenses for surface waves, refracting them toward the central jet and substantially enhancing wave height—and thus steepness—in the counter-current region. The presence of the dipole broadens the wave spectra in both frequency and directional space, with the magnitude of this broadening modulated by the initial directional spreading of the waves.

## 1. Introduction

Eddy dipoles, often referred to as mushroom-like eddies, are ubiquitous mesoscale features in the global oceans. In contrast to isolated eddies, eddy dipoles consist of a coupled cyclonic–anticyclonic pair that generates a narrow, high velocity central jet (Fedorov and Ginsburg, 1986; Fedorov et al., 1989). This configuration produces stronger current gradients and enhanced vorticity compared to a single eddy. As a result, wave–current interactions are more pronounced, particularly through increased refraction and wave energy focusing. While commonly associated with strong currents like the Gulf Stream, eddy dipoles also emerge in weaker flow regimes, indicating that their formation is not solely dependent on background flow intensity (Beron-Vera et al., 2008).

Through the transport of heat, nutrients and energy, eddy dipoles contribute substantially to shaping the spatial distribution of oceanic temperature and salinity. The intensified surface currents within their central jets, though spatially confined, can markedly enhance local energy exchanges and associated processes (Apango-Figueroa et al., 2015; Vianello et al., 2020; Malan et al., 2020; Ni et al., 2020). Such effects are particularly pronounced when the jet interacts with opposing wave systems, creating local striking dynamical imbalances.

---

* Corresponding author.
*E-mail address:* felipe.santos@noc.ac.uk (F.M. dos Santos).

https://doi.org/10.1016/j.dsr.2026.104704
Received 18 September 2025; Received in revised form 19 April 2026; Accepted 18 May 2026

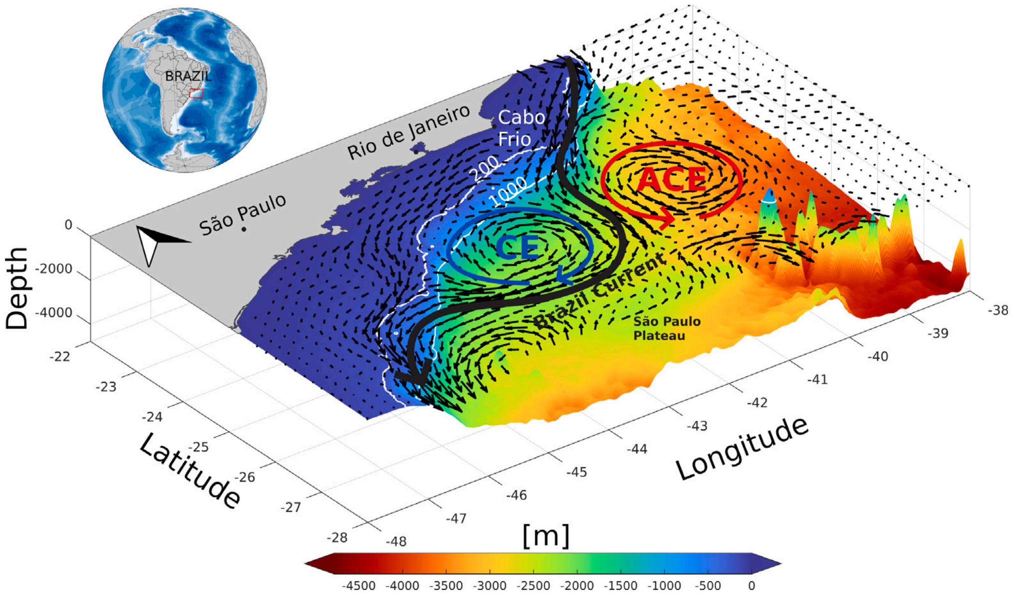

**Fig. 1.** Bathymetry, key topographic features and main surface circulation, illustrating a typical eddy dipole composed of a cyclonic eddy (CE) and an anticyclonic eddy (ACE).

In the Southwestern Atlantic, eddy dipoles frequently form near 23°S (Fig. 1), embedded within the Brazil Current (BC). This region is characterized by abrupt coastline variations and steep topography, which strongly affect the surface circulation of the Southeast Brazilian Bight and the Sao Paulo Plateau. Its importance is further underscored by its role as an oil and gas exploration frontier and a hub for maritime traffic along Brazil's southeastern coast. The BC's vigorous mesoscale activity often generates dipoles accompanied by strong vertical shear and baroclinicity (Calado et al., 2008; Arruda and Silveira, 2019; de Paula et al., 2025). These structures typically manifest as recurrent cyclonic–anticyclonic eddy pairs, as depicted schematically in Fig. 1. Of particular interest is the south-southwestward propagation of these dipoles (de Paula et al., 2021), whose central jets generate surface currents opposing the dominant north-northeastward swell (Violante-Carvalho et al., 2004). This configuration induces localized wave energy amplification, triggering our interest into how wind generated waves respond to such complex flow conditions.

Surface currents are accounted for in WW3 through the wave action balance equation (WW3DG, 2019), where they modify wave propagation via refraction and advection, as well as the intrinsic wave frequency. These processes affect wave height, direction and spectral shape. Recent studies have shown that mesoscale spatial variability in significant wave height (Hs) is primarily controlled by current induced refraction (Ardhuin et al., 2017; Romero et al., 2017; Quilfen et al., 2018; Violante-Carvalho et al., 2025). As a result, gradients in Hs are closely linked to the vorticity structure of the underlying current field.

This problem presents practical challenges. A robust analysis requires a well-developed dipole with a distinct central jet and an opposing wave system aligned along the same axis. Furthermore, observational confirmation requires a satellite ground track oriented along the dipole's central axis. This enables retrieval of full directional wave spectra from SAR wave mode imagettes—rather than relying on integrated parameters such as significant wave height from altimeters. These stringent criteria required a comprehensive search through available datasets to identify an appropriate event. To our knowledge, this study provides the first detailed analysis of spectral wave transformations measured across an eddy dipole's central jet. Therefore, this study aims to quantify the spectral transformation of swell induced by eddy dipole central jets, using SAR wave mode imagettes and wave–current simulations.

The paper is organized as follows: Section 2 outlines the data and methodology, subdivided into HYCOM (Section 2.1) and WW3 (Section 2.2) model descriptions, altimetry-based dipole detection (Section 2.3) and SAR wave-spectra inversion (Section 2.4). Section 3 presents idealized simulations of wave–current interactions, while Section 4 examines a real case, covering dipole dynamics (Section 4.1) and observed spectral changes (Section 4.2). Finally, Section 5 synthesizes the conclusions.

## 2. Data and methodology

### *2.1. Ocean model data*

Data from the Global Ocean Forecasting System (GOFS) 3.1, developed by the HYCOM Consortium in collaboration with the Navy Coupled Ocean Data Assimilation system (HYCOM+NCODA), were used to numerically investigate wave–current interaction, focusing specifically on the influence of currents on the wave field. The HYCOM NCODA GOFS 3.1 ocean reanalysis, hereafter referred to as HYCOM, has a horizontal resolution of 1/12° and 41 vertical layers. It assimilates altimeter observations, *in situ* sea surface temperature measurements and vertical temperature and salinity profiles from XBTs, Argo floats and moored buoys.

A single snapshot of surface velocity components from experiment 53.X (shown in Fig. 2a corresponding to 05Sep2010 00:00 UTC), was selected to provide the surface current field for the idealized simulations discussed in Section 3. This particular date was chosen due to the presence of an eddy dipole over the Sao Paulo Plateau, which resulted in an intensified current along its central jet, as described in detail by de Paula et al. (2021). In that study, comparisons between near-surface velocities from a regional simulation, global reanalyses and observations from a mooring deployed along the dipole's central axis demonstrated that HYCOM successfully reproduced the current magnitude. Specifically, the southward current along the central jet reached approximately 1 $\mathrm{m\,s^{-1}}$ at 42.88°W and 25.88°S. The spatial signature of the dipole in the HYCOM sea surface height field was clear and consistent with satellite altimetry. Additionally, the event illustrated in Fig. 2a is particularly suitable for this analysis because the central jet exhibits a well-defined, straight north–south orientation, free from strong longitudinal meanders that would otherwise complicate the interpretation.

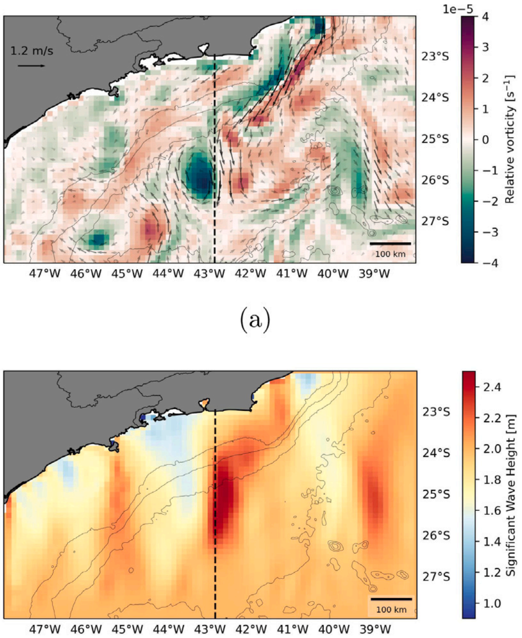

(a)

(b)

**Fig. 2.** (a) Surface current speed and direction (arrows) from a HYCOM run for 05Sep2010 and associated relative vorticity, employed in the simulations discussed in Section 3. (b) Spatial distribution of significant wave height ($H_s$) for northward waves—run R1 (Table 1), with currents included. The dashed vertical line is a transect along the maximum current velocity on the dipole central jet.

## 2.2. Wave model WW3 setup

Idealized simulations of waves propagating across eddy dipoles were performed using WW3 version 6.07, configured with a spectral grid of 48 directions ($\Delta\theta = 7.5°$) and 32 frequencies exponentially spaced from 0.0373 Hz to 0.7159 Hz, with an increment factor of 1.1. The ST4 source term package (Ardhuin et al., 2010) was employed—model configuration, governing equations and bulk parameters are thoroughly described in WW3DG (2019).

The computational grid had a horizontal resolution of 0.125° in both $\Delta x$ and $\Delta y$, covering the region from 48°W to 38°W and 28°S to 22°S in the Southwestern Atlantic (Fig. 2), with bathymetry from the ETOPO1 dataset (Amante and Eakins, 2009). The primary focus of the analysis in Section 3 is the central jet of the dipole, approximately spanning 27°S to 25°S along the transect shown in Fig. 2, located in deep waters exceeding 2000 m water depth.

All simulations used a JONSWAP frequency spectrum and a cosine-2s directional spreading function (Massel, 2017). Based on spectral parameter analysis and comparisons with measured narrow-band swell spectra, Lucas and Guedes Soares (2015) demonstrated that the JONSWAP model better describes the swell spectrum than the Gaussian model. Therefore, the JONSWAP spectrum was used as the initial condition in all simulations.

Two distinct steepness values ($\epsilon = H_s/2k_p$, where $H_s$ is the significant wave height and $k_p$ is the peak wavenumber) and three directional spreading values ($\sigma$) were considered—summarized in Table 1. Runs R1 and R2 represent swell generated by distant storms, characterized by lower steepness and narrower directional spreading. Runs R3 and R4 represent swell generated comparatively closer to the domain, with higher steepness and broader directional spreading. An example of the $H_s$ spatial distribution of run R1 is shown in Fig. 2b, where a distinct increase in wave height is observed along the central jet of the dipole.

**Table 1**
Initial state of WW3 simulations with distinct values of Significant Wave Height ($H_s$), Peak Period ($T_p$), steepness ($\epsilon$) and directional spreading ($\sigma$). In all runs the waves propagate northward ($\theta = 180°$).

| *Run* | $H_s$ (*m*) | $T_p$ (*s*) | $\epsilon = \frac{H_s}{2} k_p$ | $\sigma$ (°) |
|---|---|---|---|---|
| *R*1 | 2 | 15 | 0.018 | 15 |
| *R*2 | 2 | 15 | 0.018 | 30 |
| *R*3 | 4.4 | 9 | 0.109 | 30 |
| *R*4 | 4.4 | 9 | 0.109 | 47 |

To focus on the current-induced modifications of the wave spectra, wind forcing was excluded from the simulations. Including wind forcing would introduce additional complexity that would alter the scope of the present analysis. For runs R1 and R2, due to their lower steepness, dissipation and nonlinear wave–wave interactions were expected to be negligible. However, these processes may be significant in runs R3 and R4 and were therefore activated in all cases described in Table 1. Waves propagated northward ($\theta = 180°$) from the southern boundary, approximately 100 km south of the dipole. Each simulation was run for 48 h, sufficient for the wave field to reach a steady state across the computational domain.

Two scenarios were designed to investigate the effects of dipole-induced currents on wave propagation. The first scenario, using HYCOM surface currents (Fig. 2a), assumed a stationary current field during the wave model run. This approximation is reasonable given the relatively slow evolution of ocean eddy dipoles, as further discussed in Sections 2.3 and 4.1 and in de Paula et al. (2021). The second scenario was a control case without currents. In total, eight runs were performed (Table 1), encompassing different combinations of steepness and directional spreading.

## 2.3. Eddy dipole search criteria from altimeter data

Delayed-time merged absolute dynamic topography (ADT) and derived absolute surface geostrophic velocities, obtained from the SSALTO/DUACS multi-mission altimeter data processing system (hereafter SSALTO/DUACS), were employed to identify oceanic eddy dipoles. A dipole can be characterized as a pair of adjacent eddy-like features with contrasting ADT values—positive anomalies associated with anticyclonic eddies and negative anomalies with cyclonic eddies. The ADT is computed as the sum of the sea level anomaly (SLA) and the mean dynamic topography (MDT), according to:

$$ADT\,(x, y, t) = SLA\,(x, y, t) + MDT\,(x, y, t)\,. \qquad (1)$$

The DUACS products are referenced to a 20-year climatology spanning 1993–2012. The ADT and surface geostrophic velocities are distributed by the Copernicus Marine and Environmental Monitoring Service (CMEMS) as daily products with a horizontal resolution of 1/4°. In this study, we used the "cmems_obs-sl_glo_phy-ssh_my_allsat-l4-duacs-0.25deg_P1D" product, a Level 4 dataset containing gridded fields from multiple satellite missions. CMEMS also provides equivalent near-real-time products with the same spatial and temporal resolutions. These products combine geostrophic currents derived from variations in sea surface height, integrating data from missions such as Jason and Sentinel-3, thereby generating a comprehensive and consistent global surface current dataset.

By applying the proposed search criteria over the 1993–2021 period, we identified 115 dipole events (Fig. 3a). Altimetry-derived ADT maps were analyzed daily to reliably detect dipole formation, which we defined as the interaction of a frontal meander of the Brazil Current with an anticyclonic eddy. Once a dipole was formed and a distinct central jet developed between the eddy cores, the event was stored for subsequent analysis. In most cases, dipoles formed between the 200 and 3000 m isobaths and propagated south-southeastward or westward.

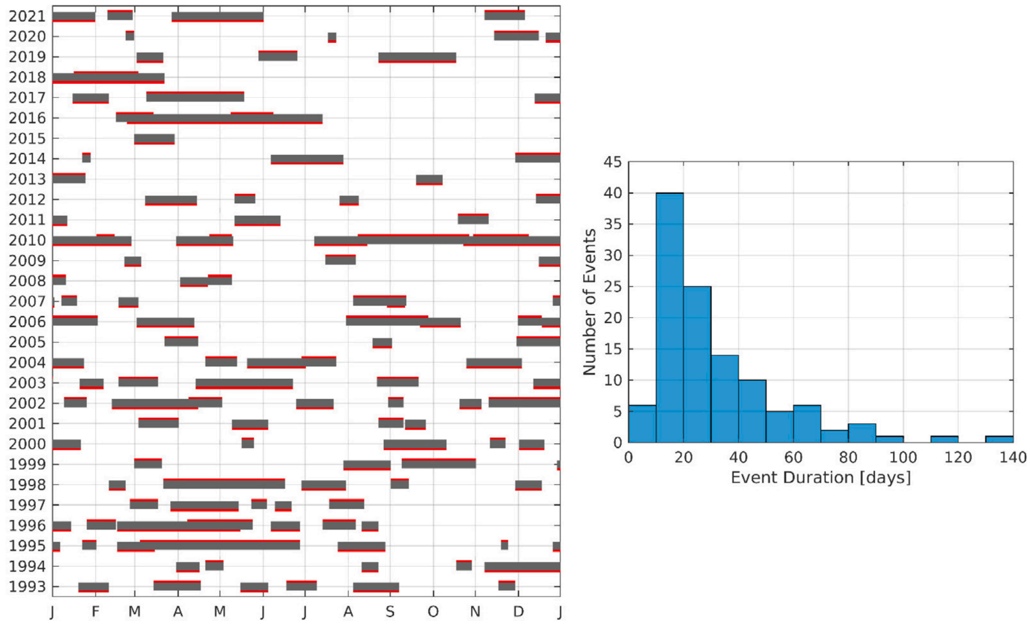

**Fig. 3.** Occurrence of dipoles in the Southwestern Atlantic, between 1993 and 2021 (see also Fig. 1). A total of 115 eddy dipole events were identified in the 22–30°S region using satellite altimetry data. (a) Individual red bars indicate timing and duration of each event, the gray lines are the integrated dipole events. (b) Histogram of events against duration (life span of dipoles) indicates that most of the dipoles get diffused within 3–6 weeks.

Occasionally, a dipole would dissipate and the same cyclone could subsequently interact with another anticyclone to form a new dipole.

The lifetimes of short-lived dipoles ranged from 5 to 21 days (Fig. 3b), while long-lived dipoles persisted between 21 and 42 days. As illustrated in Fig. 3b, long-lived dipoles were relatively rare. The eddy-like features associated with the 115 events exhibited mean diameters of 150 ± 40 km, with observed values ranging from 90 to 330 km. No clear seasonal pattern in dipole formation was observed, although between 1993 and 2010, an average of 4 to 6 dipole events occurred annually. Remarkably, two dipoles were observed to persist for more than four months. After 2011, however, a decrease in the frequency of events was noted.

### *2.4. SAR retrieved wave directional spectra*

Analyzing spectral changes associated with the interaction between waves and the central jet of an eddy dipole requires accurate measurements of directional wave spectra (dos Santos et al., 2025). Satellite-borne Synthetic Aperture Radar systems provide an ideal data source for this purpose (see, for example, Violante-Carvalho et al. 2005, Ardhuin et al. 2009, Violante-Carvalho et al. 2012, Asiyabi et al. 2023, Owda et al. 2024. The Envisat SAR datasets are publicly available through the European Space Agency (ESA) repository: https://earth.esa.int/eogateway/missions/envisat. Envisat SAR images were selected for this study instead of the more recent Sentinel-1 dataset due to Envisat's extensive archive, comprising millions of calibrated complex look imagettes. The Wave Mode (WV) product from Envisat achieves global ocean coverage at high spatial resolution and includes specialized outputs for wave analysis: Imagette and power spectrum (WVI), Image Cross-Spectra (WVS) and Ocean Wave Spectra (WVW). These products provide high-quality data, typically offering comprehensive and reliable wave spectral information. A minor, though sometimes relevant, limitation is the directional ambiguity sometimes present in the WVW product (Portilla-Yandún et al., 2019; Li et al., 2021). To address this issue, Brasil-Correa et al. (2022) proposed an alternative approach capable of removing such ambiguities, which is particularly relevant for our application.

A novel inversion scheme for retrieving wave spectra from SAR images, referred to as the Linear Inversion Method (LIM) was fully described in Brasil-Correa et al. (2022). For completeness, its main features are briefly summarized here. LIM is an efficient and computationally inexpensive algorithm that processes the Image Cross-Spectra acquired from homogeneous imagettes over deep waters. Compared to classical inversion methods (such as Hasselmann and Hasselmann 1991, Krogstad et al. 1994, Engen and Johnsen 1995, Hasselmann et al. 1996, Bao and Alpers 1998, Mastenbroek and de Valk 2000, Chapron et al. 2001, Schulz-Stellenfleth and Lehner 2005, Collard et al. 2009), LIM has the additional advantage of not requiring *a priori* information—typically provided by wave or meteorological models—to retrieve the directional wave spectrum.

Nonlinear effects are not explicitly accounted for in LIM. To address this, Brasil-Correa et al. (2022) introduced empirical corrections based on key wave parameters, such as significant wave height, peak period and peak direction. Using the simulator described in Santos et al. (2021), unimodal sea states and their corresponding simulated SAR spectra were generated and inverted using LIM to produce directional wave spectra. The differences between these simulated (input) and retrieved spectra were used to develop post-processing correction factors.

The implementation of this improved system involved integrating a spectral partitioning scheme into the WVS processing routine. Each cross-spectral partition was inverted individually and corrected—consistent with the unimodal correction approach—before linearly combining them to obtain the final multimodal spectrum. In addition, filtering routines were incorporated to remove noise, high-frequency distortions and non-wave low-frequency features from the SAR cross-spectra, thereby enhancing the accuracy of the retrieval. These filtering procedures are broadly based on the pre-processing methods described in the Northern Research Institute (NORUT) reports (Johnsen et al., 2006-10-24).

In operational terms, the processing workflow begins with downloading the desired SAR products, discarding inhomogeneous imagettes and applying the pre-processing filters. The LIM inversion is then performed, followed by the calculation of wave spectral parameters and the application of empirical corrections, including rescaling, rotation and wavelength shifts. As a result, a post-processed directional wave spectrum is retrieved, with nonlinear effects compensated through the use of empirical lookup tables.

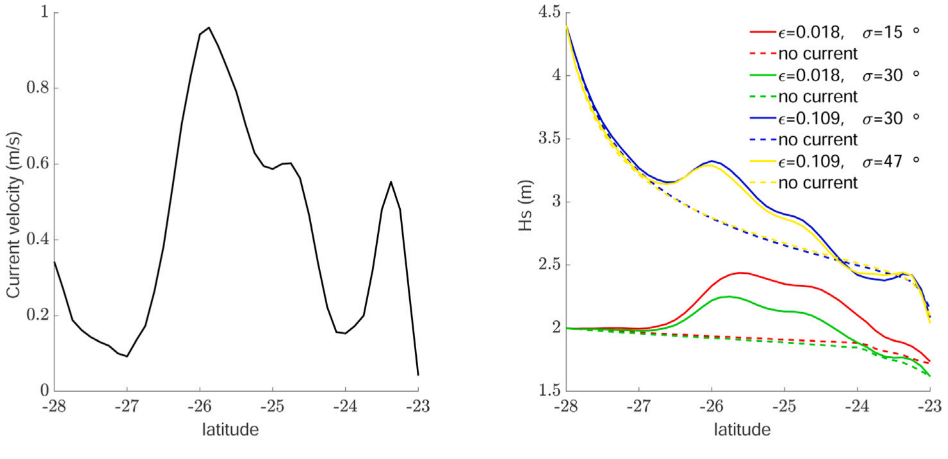

(a) (b)

**Fig. 4.** (a) Current velocity (southward) along the transect depicted in Fig. 2a. (b) Significant wave Height ($H_s$) along the transect. The colors from red to yellow are, respectively, runs $R1$ to $R4$—Table 1. Runs without current are shown as dashed lines.

It is important to note the conceptual distinction between $H_s$ estimation in LIM and in the ESA-distributed WVW spectra. The WVW approach applies lookup tables to rescale the entire directional spectrum based on SAR image parameters (Johnsen et al., 2006-10-24). In contrast, LIM applies empirical corrections derived from numerical simulations to adjust biases in the retrieved directional wave spectrum itself, accounting for the neglected nonlinear interactions (Santos et al., 2021; Brasil-Correa et al., 2022). In Section 4.2, we employ SAR directional wave spectra retrieved using LIM from an Envisat ground track segment crossing an eddy dipole in the Southwestern Atlantic to assess the impact of the central jet on opposing wave systems.

## 3. The effects of currents on waves in an ocean eddy dipole using idealized simulations

Idealized numerical experiments were conducted to investigate the interaction of surface waves with an oceanic eddy dipole and its intensified central jet. These simulations provide a controlled framework for analyzing the primary physical processes before addressing more complex, real-world cases. The present simulations do not include two-way wave–current coupling, and therefore may not capture cumulative feedback effects. However, they provide a controlled framework to isolate the primary influence of current-induced refraction on wave spectral properties.

Previous studies have examined wave–current interactions across a range of scales and configurations (Ardhuin et al., 2012, 2017; Quilfen et al., 2018; Romero et al., 2017, 2020; Bôas et al., 2020; Lauton et al., 2023; Violante-Carvalho et al., 2025). However, the role of directional spreading in modulating these interactions remains less thoroughly addressed (Violante-Carvalho et al., 2021). The present analysis considers waves propagating against the central jet of a dipole, under varying directional spreading and steepness conditions, in order to assess how these spectral properties influence the interaction dynamics.

Additional sensitivity tests were performed by altering the maximum velocity of the central jet. These experiments showed that variations in current intensity primarily affect the magnitude of the wave response, while the qualitative interaction patterns remain unchanged. For this reason, only one representative case is presented in the following analysis, as it sufficiently illustrates the essential features of the interaction between the current and the opposing wave field.

Numerical simulations in the Agulhas Current region by Marechal and Ardhuin (2021) demonstrated that narrower directional spreading leads to larger gradients in significant wave height. This effect is illustrated in Fig. 4, which shows the variations in $H_s$ (along the transect shown in Fig. 2) for different WW3 simulations—as described in Section 2.2. For runs R1 and R2 (shown in red and green in Fig. 4b, both with identical steepness), narrower directional spreading results in a more pronounced increase in $H_s$ within the region of steep current gradients. Specifically, in the area with the sharpest variation in current speed (Fig. 4a), the maximum increase in $H_s$ relative to the run without currents reaches 27% for $\sigma = 15°$ and 17% for $\sigma = 30°$. A similar dependence on directional spreading is observed for the steeper waves in runs R3 and R4 (blue and yellow), although the effect is somewhat less pronounced. In these cases, the maximum enhancement of $H_s$ in opposing currents is approximately 16% for $\sigma = 30°$ and 15% for $\sigma = 47°$.

Currents modify wave propagation direction at a given location through both refraction and wave action advection. The amount of deviation from the great-circle path depends not on the current speed itself but on the ratio between the vertical component of the current vorticity ($\zeta$) and the wave group velocity ($c_g$), following the relation:

$$\chi = \frac{\zeta}{c_g} + O(\epsilon^2), \tag{2}$$

where $\chi$ is the ray curvature, $\zeta = \frac{\partial v}{\partial x} - \frac{\partial u}{\partial y}$ is the vertical component of the surface current vorticity and $\mathbf{U} = (u, v)$ represents the horizontal components of the surface current. The parameter $\epsilon = \|\mathbf{U}\|_2/c_g$ expresses the ratio of current speed to group velocity. A comprehensive discussion of this relationship, derived from ray theory, can be found in Kenyon (1971) and Dysthe (2001). The direction of wave bending follows the sign of the vorticity field, with the magnitude of the deviation increasing as the vertical vorticity of the current increases.

Ocean eddy dipoles act as focal lenses for surface gravity waves, refracting the wave energy toward the central jet region (Fig. 5). Dipoles are rarely symmetrical with respect to the central jet axis. This asymmetry is exemplified in the case shown in Fig. 2a and the corresponding zoomed view in Fig. 5, where the clockwise eddy exhibits a comparatively larger (negative) relative vorticity.

The numerical simulations reproduced also the changes in peak wave direction as waves propagated through the dipole region (Fig. 6a). These directional changes were also influenced by the initial directional spreading of the wave field. In the area of steepest current gradients, the deviation in peak direction relative to the run without currents was greater for waves with narrower directional spreading. For example, in runs R1 and R2 (red and green, respectively), both initialized with the same steepness, the maximum directional shift reached approximately

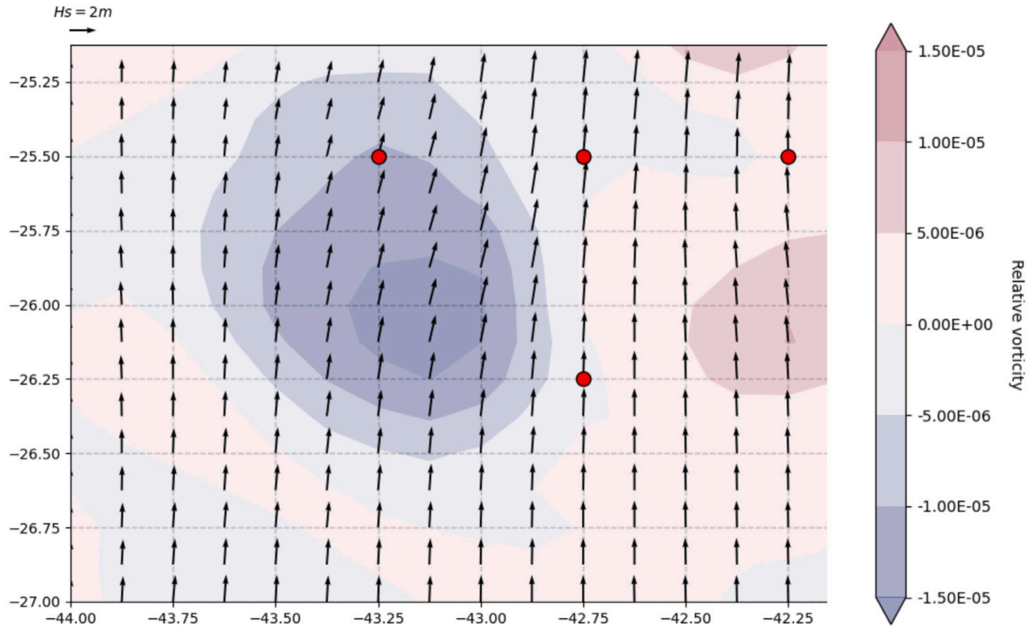

**Fig. 5.** Peak direction in the dipole region for run $R1$ (Table 1); the length of the vectors is proportional to $H_s$. Also shown the contour lines of the relative vorticity field, with negative values as blue and positive as red. The red dots are the grid positions of the spectra shown in Fig. 7.

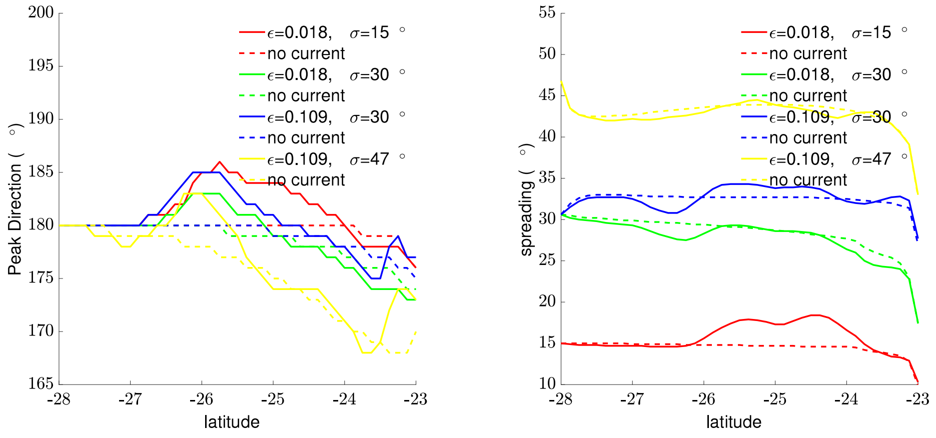

(a) (b)

**Fig. 6.** (a) Peak direction and (b) directional spreading $\sigma$ along the transect. Runs without current are shown as dashed lines.

6° for the narrower spreading case ($\sigma$ = 15°, R1) and about 3° for the broader spreading ($\sigma$ = 30°, R2). A similar dependence on directional spreading was observed in runs R3 and R4, where narrower directional spreading again resulted in larger deviations in peak direction. These results indicate that a narrow initial directional spreading, such as $\sigma$ = 15°, enhances the refraction of the wave peak direction as the waves cross the dipole region.

The directional spreading of the wave field is also modified by the presence of the dipole (Fig. 6b), as wave refraction alters both the propagation direction and the directional distribution. The simulation with the initially narrower spreading (R1) exhibits the most pronounced broadening, particularly along the central jet, where $\sigma$ increases by up to 26% relative to its initial value. In contrast, the broadening of $\sigma$ in runs R2, R3 and R4 is comparatively smaller, reflecting the reduced sensitivity of initially broader directional spectra to current-induced refraction.

To better illustrate the changes in propagation direction and the broadening of the wave spectrum induced by the central jet, Fig. 7 presents directional spectra at four selected grid points at a single time step. Points (a) and (b) are located along the central transect, respectively upstream of the region of maximum current speed (26.25°S, 42.75°W) and further north at the location where the directional spreading $\sigma$ reaches its maximum (25.50°S, 42.75°W). Points (c) and (d) are positioned adjacent to point (b), respectively at 25.50°S, 43.25°W (closer to the anticyclonic eddy) and 25.50°S, 42.25°W (closer to the cyclonic eddy)—the positions of the spectra are shown in Fig. 5. Both eddies contribute to refracting the incoming wave energy toward the central jet region. As shown by the comparison between Figs. 7a and 7b, this refraction substantially increases the directional spreading. The most pronounced change in wave direction is induced by the anticyclonic (clockwise) eddy (Fig. 7c), which exhibits greater relative vorticity. Wave direction is deflected toward the central jet, where it merges with the wave components refracted by the cyclonic eddy. This convergence results in a broadened spectrum, both in frequency and direction, as evidenced in Fig. 7b.

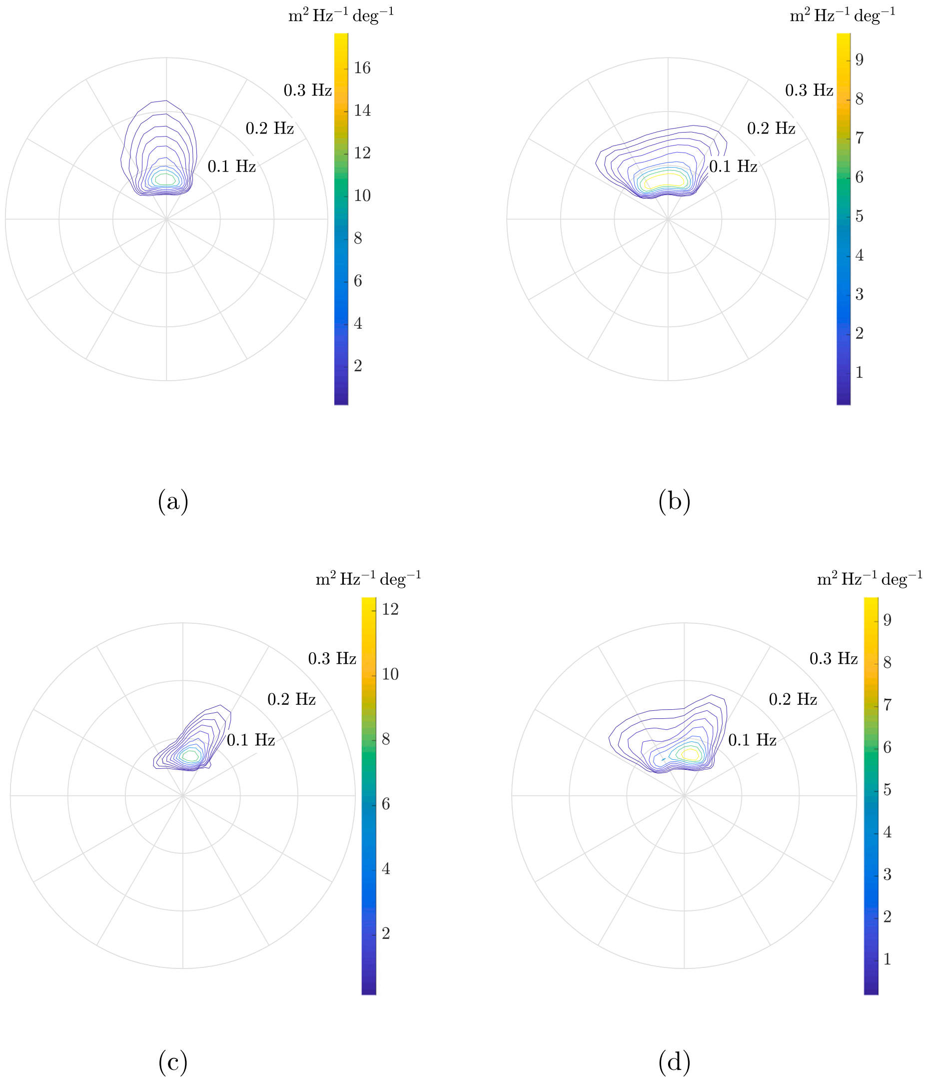

(a) (b)

(c) (d)

**Fig. 7.** Directional spectra on four grid points at the same computational time for run $R1$; (a) 26.25°S and 42.75°W; (b) 25.50°S and 42.75°W; (c) 25.50°S and 43.25°W; (d) 25.50°S and 42.25°W—their positions are depicted in Fig. 5. The concentric circles denote frequency at 0.1 Hz interval starting at 0.1 Hz (inner) till 0.3 Hz (outer circle). Employing the same orientation used in the LIM, i.e. where the waves are going to.

## 4. Case study: Ocean eddy dipole in the Sao Paulo Plateau, Southwestern Atlantic

Following the idealized simulations, the analysis focuses on a selected real-world event that satisfies three critical criteria: the presence of a well-defined eddy dipole with an intensified central jet, waves propagating in opposition to the current and the passage of a SAR satellite ground track aligned with the central jet axis—where wave–current interactions are most pronounced. The integration of satellite observations with numerical simulations provides a robust framework for evaluating these interactions in detail. Among the many dipoles identified within the study area (Fig. 3), only a few fulfilled all the conditions necessary for detailed analysis. Although the selected ground tracks did not coincide with an extreme wave event, it offers a representative and well-characterized configuration. *Mutatis mutandis*, the conclusions drawn here are applicable to more energetic situations. The following analysis focuses on the most illustrative of these cases.

### *4.1. Formation and evolution of the eddy dipole*

The evolution of the ADT fields prior to the 28Feb2004 selected event is shown in Fig. 8. To better understand the origin of the observed dipole, it is essential to examine the surface circulation patterns leading up to this date and to characterize the sequence of dynamical processes responsible for its formation. The approximate locations of the cyclonic (low ADT) and anticyclonic (high ADT) features that comprise the eddy dipole are indicated by yellow circles, while their trajectories over the examined period are shown as black lines. The formation of this dipole appears to result from the interaction between a meander of the BC, marked by a low/blue ADT region and a pre-existing anticyclonic feature, marked by a high/red ADT region.

In the preceding weeks, both the cyclonic and anticyclonic features propagated southwestward, following the general flow direction of BC. The cyclonic eddy advanced more rapidly than its anticyclonic counterpart, likely due to the advective influence of the BC along the continental slope. This behavior is consistent with the eddy propagation statistics reported by Silveira et al. (2023) and corresponds well with the trajectories shown in Fig. 8. By the end of the period, the two opposing circulation features evolved into an asymmetric eddy dipole, characterized by a central jet oriented toward the south-southeast and containing the strongest surface currents within the domain. Surface velocities exceeded 0.6 m s$^{-1}$ in the northwestern sector of the dipole and along its central jet, where the ADT gradients were highest and the cyclonic and anticyclonic cores were in closest proximity.

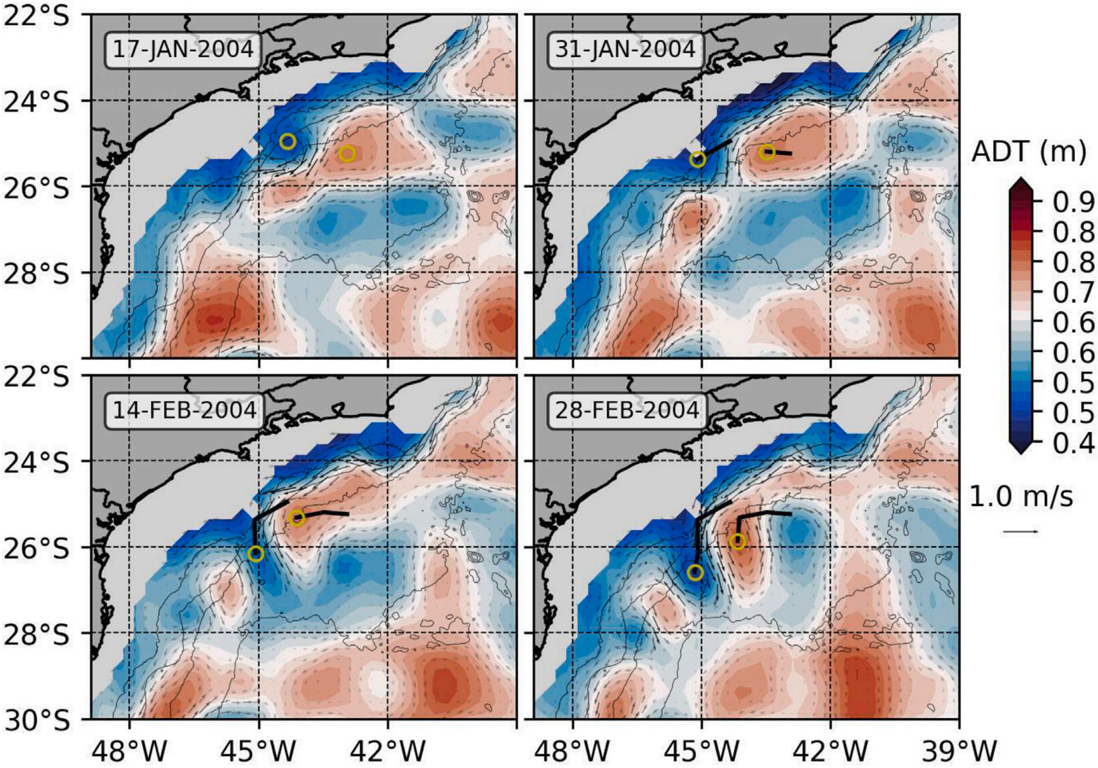

**Fig. 8.** Sequence of daily ADT fields and associated surface geostrophic currents prior to 28Feb2004. The yellow circles indicate the approximate positions of the high and low sea surface elevation cores that form the dipole. The black lines show the trajectory of the cores from the first instant shown. Data at depths less than 100 m were masked.

Fig. 9 presents a detailed dynamical snapshot of the study area on 28Feb2004—the red square marks the region of maximum surface velocity. It is important to note that the precise position of the eddies and consequently the location of the velocity maximum, may be subject to uncertainty due to the inherent spatial and temporal resolution limitations of the gridded SSALTO/DUACS altimetry dataset. For this particular date and region, the formal mapping error in sea surface height ranges between 0.01 and 0.05 m, implying a similar level of uncertainty in the ADT fields. Operational ocean models such as HYCOM (among others) assimilate altimeter data and provides global forecasts of ocean currents, typically with 1/12° horizontal resolution. However, the positioning of the mesoscale features on these forecasts may not be sufficiently accurate due to model uncertainties—for instance subgrid parametrizations, data availability for assimilation, assimilation scheme, to name a few. Therefore, the ability of global ocean forecasts to precisely locate eddy dipoles, which is critical for the accuracy of wave model predictions for safer maritime operations, may vary over time. On the other hand, near real time data from SSALTO/DUACS provides precise observations of the position of mesoscale features on a daily basis, though at lower resolution (1/4°) and with only the geostrophic component of the current. However, typical length ($L$) and velocity scales ($U$) of eddy dipoles are 100 km and 1 m s$^{-1}$, respectively. With Coriolis frequencies $f_0$ in the order of $10^{-5}$ to $10^{-4}$ s$^{-1}$, geostrophic dynamics is expected to be important or even dominant since the Rossby Number, $R_o = U/f_0 L$, is equal or less than 1. Hence, although gridded altimetry may underestimate total current components of eddy dipole events, it might provide a more accurate representation of the dipoles position and evolution, making it a preferred choice for the analysis of a specific event and for nowcast purposes (Violante-Carvalho et al., 2025).

The characteristic spatial and temporal scales of the mesoscale features analyzed here are typically on the order of several hundred kilometers and several weeks, respectively (Calado et al., 2006; Rocha et al., 2014; Goes et al., 2019; Silveira et al., 2023). Moreover, mooring observations reported by de Paula et al. (2021) demonstrated strong agreement in both timing and location between in situ measurements of current intensification and the central jet of the dipole inferred from satellite altimetry. These findings support the conclusion that the SSALTO/DUACS dataset provides sufficiently accurate information to investigate the influence of eddy dipole surface currents on wave transformations.

### 4.2. SAR retrieved spectral wave transformations along the dipole central jet

Wind and wave conditions are taken from the European Centre for Medium-Range Weather Forecasts (ECMWF) reanalysis products, which provide a reliable representation of the large scale sea state. Notably, the ECMWF wave model does not include surface currents as input, which is particularly relevant here, as it allows the effects of currents on the wave field to be assessed independently. A full hindcast using WW3 with realistic wind forcing and time evolving currents would introduce additional uncertainties related to forcing, boundary conditions and current field representation, potentially obscuring the processes of interest discussed here. Such an approach requires high resolution, time resolved current fields with accurate dipole positioning and is therefore beyond the scope of the present study. A comprehensive hindcast analysis, applied to a different case, is presented (Violante-Carvalho et al., 2025).

To characterize the wind and wave conditions prevailing at the time and location of interest, the ERA5 atmospheric reanalysis products from the ECMWF were employed. These products, with a spatial resolution of 0.125°, are available through the Copernicus Climate Data Store (cds.climate.copernicus.eu). Notably, surface currents are not incorporated as a forcing in the ERA5 wave model configuration. The accuracy of ERA5 wave parameters has been extensively validated. Hersbach et al. (2020) reported consistent performance across multiple regions, while a more recent assessment by Wang and Wang (2022), based on

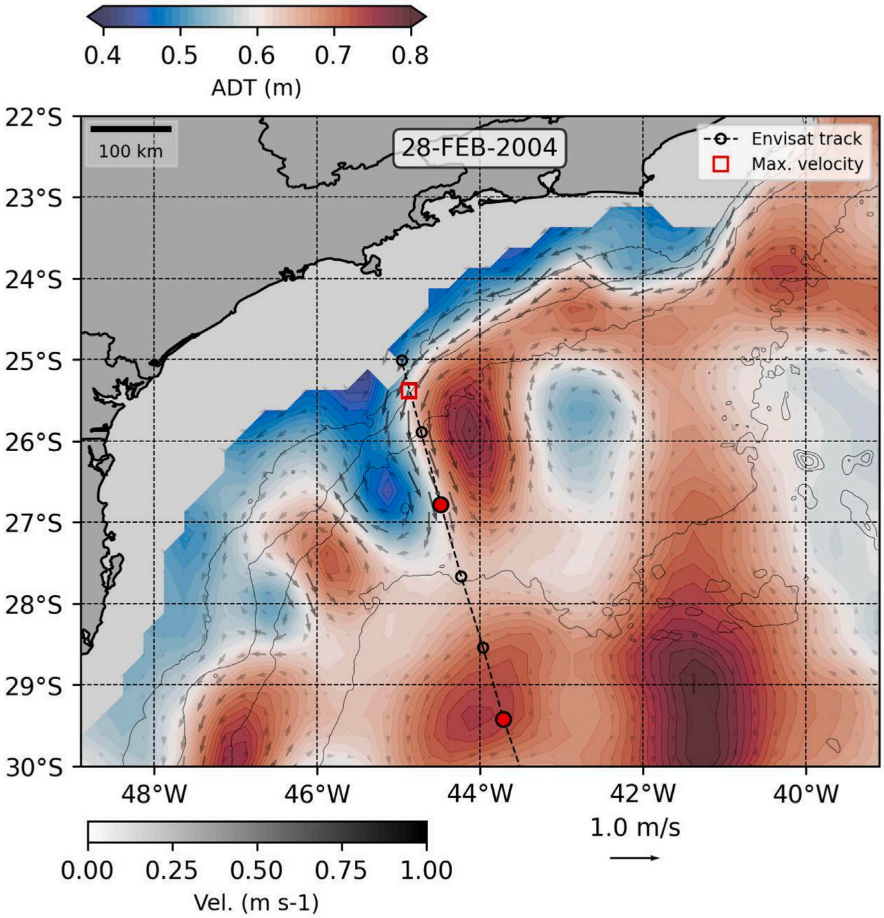

**Fig. 9.** ADT field and associated surface geostrophic velocities during the occurrence of an eddy dipole in the Sao Paulo Plateau. The eddy dipole is approximately bounded by longitudes 46°W–43°W and latitudes 25°S–28°S. The circles are the location of the SAR wave mode imagettes and the dashed line is a segment of the Envisat ascending track number 0360, on 28Feb2004 around 01:27 UTC. The red square corresponds to the point of maximum surface velocity over the entire domain. The red filled circles are the positions of the spectra shown in Fig. 13. Data at depths less than 100 m were masked.

nearly 100 wave buoys spanning a 40-year period, reported a scatter index of 0.18, a correlation coefficient of 0.96, a bias of 0.058 m and a root mean square error (RMSE) of 0.32 m for significant wave height estimates.

On February 26, a long northward fetch developed around 40°W and 60°S (Fig. 10), generating waves propagating toward the Sao Paulo Plateau. The semi-permanent South Atlantic Anticyclone (SAA) is also clearly visible in the atmospheric fields. On February 28, the center of the SAA was located near 10°W and 25°S (Fig. 10c), producing northeasterly winds over the Sao Paulo Plateau. These winds intensified in the subsequent hours, as shown in Fig. 10d.

The corresponding wave conditions, also derived from the ERA5 global reanalysis dataset, are shown in Fig. 11. On February 28, the dominant waves over the Sao Paulo Plateau were primarily propagating northward, with $T_p$ and $H_s$ of approximately 11–12 s and 1–2 m, respectively—typical values for swell along the southeastern coast of Brazil (Violante-Carvalho et al., 2004; Pereira et al., 2017). ERA5 provides mean wave direction rather than peak direction; therefore, to maintain consistency with the peak period representation and to avoid potential misinterpretation in a multi modal sea state, directional information is not included. The propagation of the windsea and swell components can be inferred from the spatial distribution of peak period and is explicitly resolved in the directional spectra discussed later in this section.

The date of 28Feb2004 was selected for analysis due to the favorable spatial coincidence between the Envisat ground track and the well-developed eddy dipole, including its central jet. Moreover, most of the Envisat SAR Wave Mode imagettes acquired along this track passed our homogeneity test, indicating reliable spectral retrievals (Brasil-Correa et al., 2022). Inhomogeneities in SAR ocean images typically occur under low wind conditions and may also be associated with phenomena such as oceanic fronts, internal waves, sea ice, oil slicks and rain cells (Schulz-Stellenfleth and Lehner, 2004).

The locations of the SAR imagettes acquired along Envisat ascending track 0360 on 28Feb2004 at approximately 01:27 UTC are shown in Fig. 9. For the event analyzed, the azimuth angle is approximately 5°, defined as the absolute difference between the wave propagation direction and the SAR azimuth (along track) direction. This near alignment enhances nonlinear velocity bunching effects, which act primarily along the azimuth direction and can lead to azimuth cutoff. However, azimuth cutoff predominantly suppresses the high frequency portion of the spectrum, where orbital velocities are larger and nonlinear distortions are stronger. The long period swell analyzed here lies well above the typical azimuth cutoff scale for Envisat Wave Mode imagery (Violante-Carvalho and Robinson, 2004; Santos et al., 2021). Therefore, although the small azimuth angle implies strong geometric alignment, the swell component under consideration is not significantly affected by azimuth cutoff and its directional characteristics remain reliably retrieved.

Unlike the idealized case described in Section 3, the real jet meanders longitudinally and is not perfectly aligned in the North–South direction. Along the ground track, surface currents reached maximum velocities of approximately 0.6 m s$^{-1}$ between 25°S and 27°S, flowing predominantly southward and thus opposing the incident swell (Fig.

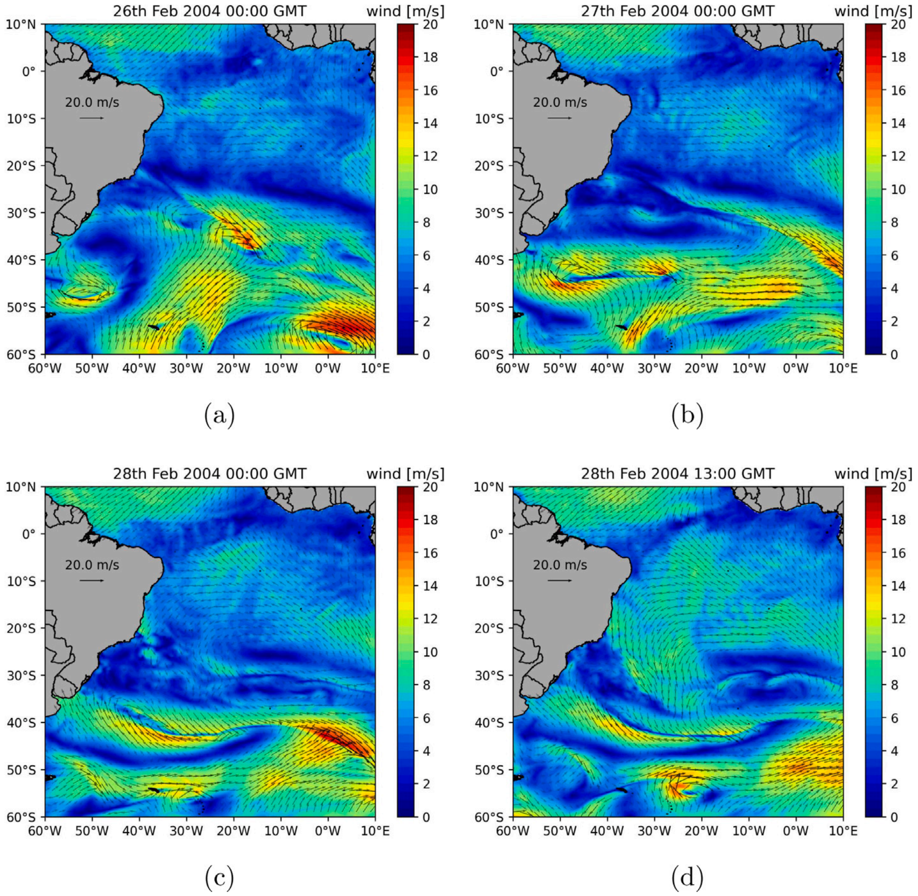

**Fig. 10.** ECMWF $U_{10}$ wind field four days prior to the case study time.

12, left). The resulting enhancement of significant wave height in the counter-current region is evident (Fig. 12, right), as captured by both the LIM retrieval method and the ESA WVW Level 2 product—this effect is absent from the ERA5 wave model, which does not account for surface current forcing. Both retrieval approaches reveal an increase in $H_s$ over the central jet, with maximum enhancements of 48% (LIM) and 23% (WVW), respectively. Further south, between 28°S and 30°S, where the surface currents are considerably weaker, SAR-derived $H_s$ and model estimates show reasonable agreement. In this region, LIM exhibits a slight underestimation and WVW a slight overestimation relative to the model results.

Fig. 13 presents the SAR-retrieved directional wave spectra obtained upstream and downstream of the maximum surface currents within the dipole's central jet and the corresponding SAR imagettes. To better illustrate the relative contributions of the wind sea and swell components, each spectrum is normalized by its maximum value. Upwave of the central jet (Fig. 13a and b), a swell system with a peak period of 11.2 s propagated north-northwestward, while a comparatively more energetic wind sea traveled west-southwestward. Approximately 300 km downwave, the opposing surface current substantially amplified the swell energy, which became dominant over the wind sea (Fig. 13c and d). In contrast, the wind sea component remained largely unaffected, maintaining its spectral characteristics in terms of wavelength, direction and energy. The swell was refracted northward by approximately 15°, with its peak period reduced to 10.2 s, resulting in a notable increase in wave steepness. However, the directional spreading of the swell component did not exhibit significant changes.

These results highlight two key aspects. First, they demonstrate the complex transformations experienced by SAR-retrieved directional wave spectra under opposing current conditions, occurring over relatively short spatial scales and in agreement with numerical simulations. Second, they highlight the capability of the Linear Inversion Method to reconstruct directional spectra from SAR Wave Mode imagettes. In contrast, the ESA-distributed WVW directional spectra, although providing consistent $H_s$ estimates, exhibited unresolved directional ambiguities in some imagettes—retaining both ambiguous peaks, not shown here—as previously reported by Portilla-Yandún et al. (2019), Li et al. (2021) and Brasil-Correa et al. (2022). In the present analysis, the WVW product effectively acted as an altimetric dataset, accurately capturing $H_s$ but providing less reliable results for the shape of the directional spectra. Conversely, the directional spectra retrieved with the LIM were physically consistent, both in spectral shape and in the estimated bulk parameters.

## 5. Summary and conclusions

Ocean eddy dipoles, consisting of adjacent counter-rotating eddies, are among the most widespread mesoscale features and are potentially ubiquitous in the global ocean. These structures induce a circulation pattern that channels water along their central axis, forming a narrow and intensified jet. This study investigated the spectral transformations of wind-generated waves interacting with these central jets, using a combination of data from different types of radar sensors carried on satellites and numerical simulations. The impact of eddy dipoles on surface wave fields has received very limited attention (Violante-Carvalho et al., 2025). To the best of our knowledge, no study to date has specifically examined the spectral transformations they induce, either through observations or numerical simulations.

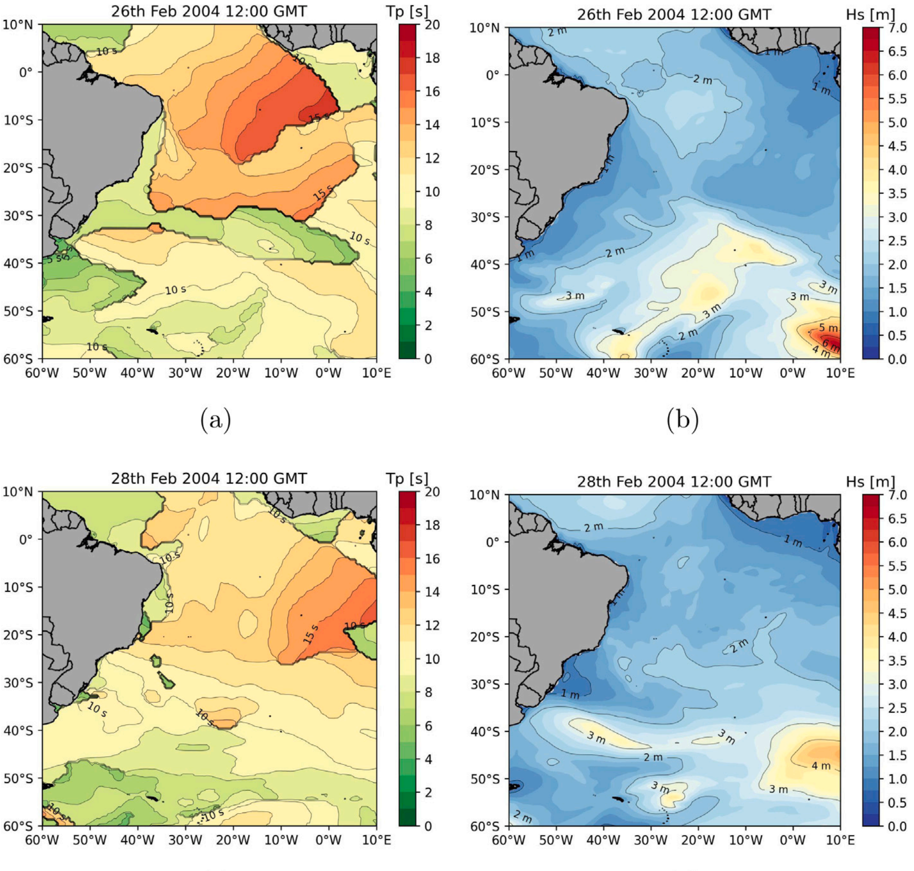

(a) (b)

(c) (d)

**Fig. 11.** ECMWF ERA5 reanalysis products: peak period ($T_p$, left) and significant wave height ($H_s$, right) fields. Top on 26Feb2004 1200 UTC and bottom on 28Feb2004 1200 UTC.

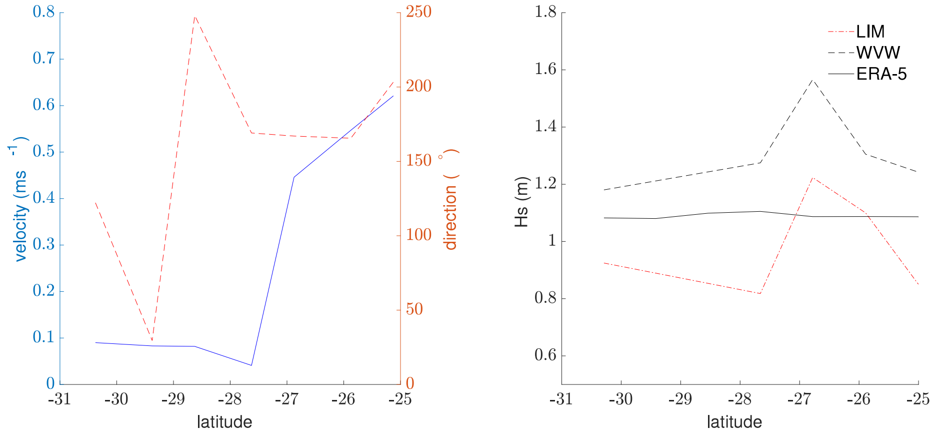

(a) (b)

**Fig. 12.** Left: surface geostrophic velocities from SSALTO/DUACS (full line in blue) and direction (dashed line in red) along the Envisat ground track depicted in Fig. 9. Right: $H_s$ along the ground track retrieved using the Linear Inversion Method (LIM), the ESA distributed WVW spectra and ERA5 spectra from the ECMWF reanalysis.

Over a hundred dipoles were identified over the Sao Paulo Plateau using delayed-time merged absolute dynamic topography and derived absolute surface geostrophic velocities from satellite altimetry. Directional wave spectra retrieved from Synthetic Aperture Radar wave mode data enabled a detailed investigation of the spectral changes induced by wave–current interactions. A specific case study was selected, in which an Envisat ground track intersected a well-defined and comparatively intense eddy dipole, providing an ideal opportunity to observe these interactions.

Idealized numerical simulations using a realistic current field and varying wave conditions were conducted to complement the SAR observations. These simulations revealed that the gradients of significant wave height ($H_s$) across the central jet are highly sensitive to the initial directional spreading of the incident waves. Narrower directional

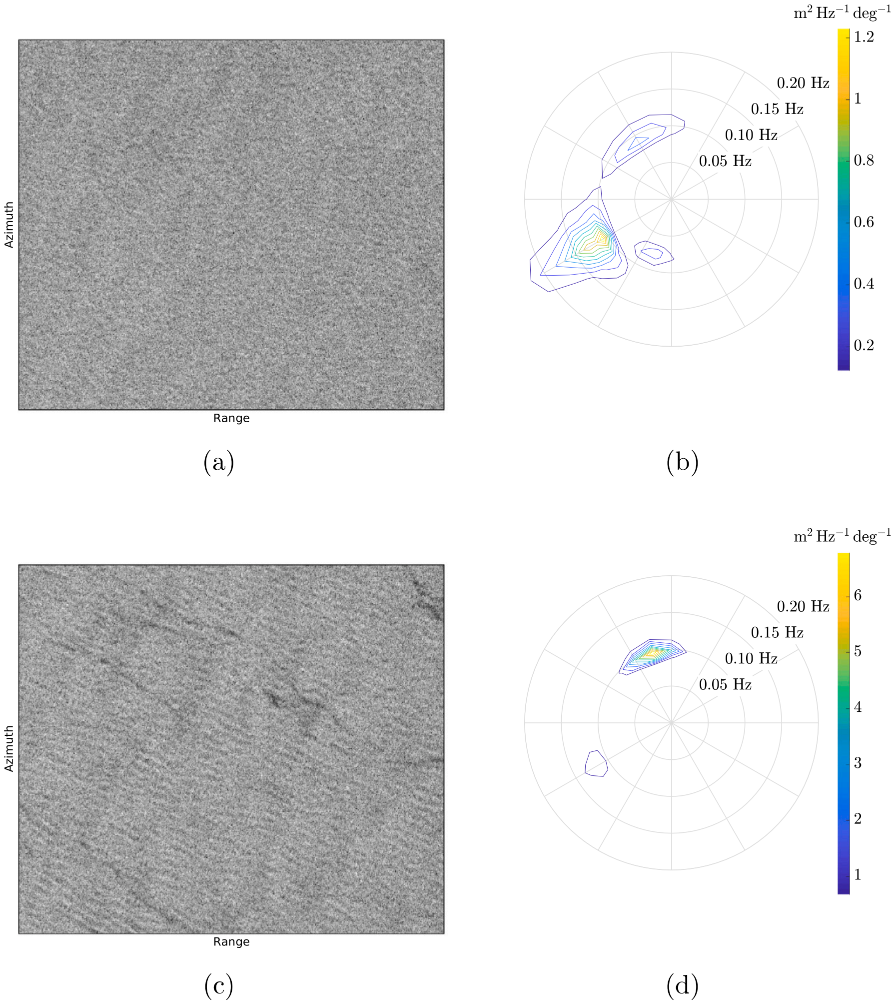

**Fig. 13.** In the right column, directional wave spectra retrieved from SAR using the LIM along the Envisat ground track at locations upwave (b) and downwave (d) of the dipole central jet, where surface velocities reach their maximum. The positions of these spectra are indicated by red filled circles in Fig. 9. Concentric circles represent frequency intervals of 0.05 Hz, ranging from 0.05 Hz at the center to 0.2 Hz at the outer circle. The left column displays the corresponding SAR Wave Mode imagettes (WVI) acquired at these locations.

spreading ($\sigma$) lead to more pronounced increases in $H_s$ and stronger spectral modifications. For instance, compared to simulations without currents, the maximum percentage increase in $H_s$ for an initial $\sigma = 15°$ is nearly twice that for $\sigma = 47°$, under a central jet current of approximately 1 $\mathrm{m\,s^{-1}}$. When the initial directional spectrum is narrow, refraction concentrates wave energy within a smaller region, leading to greater increases in wave steepness. In contrast, broader directional spectra distribute energy over a wider area, resulting in more moderate changes in wave height. The simulations also showed that the directional spreading of the spectrum increases significantly over the central jet, particularly for initially narrow spectra. Similarly, changes in peak wave direction were more substantial for narrower directional spreadings, with maximum deviations of up to 6° compared to cases without currents.

The increase in wave height in the central jet results from both the reduction in wave group velocity due to the opposing current—dynamical shoaling—and the refraction of waves converging toward the jet. Based on the simulated frequencies (Table 1) and the characteristics of the observed case, most of the wave height enhancement can be attributed to dynamical shoaling, with refraction accounting for approximately 20%–30% of the increase.

The SAR-retrieved directional spectra corroborated the numerical simulations, confirming that eddy dipoles act as focal regions for wind-generated waves, bending and converging them toward the central jet. This convergence, combined with the opposing current, significantly increases the steepness of the wave field. In the selected case, SAR observations revealed a substantial increase in $H_s$ over the central jet compared to the upwave region.

This raises the question of whether ocean eddy dipoles may enhance the occurrence of freak waves—unusually large and unexpected wave events that can be amplified by strong opposing surface currents through wave–current interactions. While steepness is markedly enhanced, the convergence of waves toward the central jet also broadens the wave spectra in both frequency and direction, especially for initially narrow directional spreadings. This broadening likely inhibits the quasi-resonant nonlinear interactions required for the formation of freak waves, which typically occur in narrow-banded conditions with a high Benjamin–Feir Index.

Nonetheless, the interaction of opposing waves with the strong currents of the central jet substantially increases wave energy, resulting in adverse sea states across a broad area. These findings suggest that ocean eddy dipoles may create hazardous navigation conditions, even if they do not directly trigger freak wave formation.

## CRediT authorship contribution statement

**Nelson Violante-Carvalho:** Writing – review & editing, Writing – original draft, Visualization, Validation, Supervision, Software, Resources, Project administration, Methodology, Investigation, Formal

analysis, Data curation, Conceptualization. **Thiago de Paula:** Writing – review & editing, Writing – original draft, Visualization, Validation, Supervision, Software, Resources, Methodology, Investigation, Formal analysis, Data curation, Conceptualization. **Leandro Calado:** Writing – review & editing, Writing – original draft, Visualization, Validation, Supervision, Software, Resources, Methodology, Investigation, Formal analysis, Data curation, Conceptualization. **Luigi Cavaleri:** Writing – review & editing, Writing – original draft, Visualization, Validation, Supervision, Software, Resources, Methodology, Investigation, Formal analysis, Data curation, Conceptualization. **Felipe Marques dos Santos:** Writing – review & editing, Writing – original draft, Visualization, Validation, Software, Methodology, Investigation, Formal analysis, Data curation. **Luiz Mariano Carvalho:** Writing – review & editing, Writing – original draft, Validation, Supervision, Software, Methodology, Investigation, Formal analysis, Data curation, Conceptualization. **Andre Luiz Cordeiro dos Santos:** Writing – review & editing, Writing – original draft, Visualization, Validation, Methodology, Investigation, Formal analysis, Conceptualization. **Alvise Benetazzo:** Writing – review & editing, Writing – original draft, Visualization, Validation, Software, Methodology, Investigation, Formal analysis, Conceptualization.

## Declaration of competing interest

The authors declare that they have no known competing financial interests or personal relationships that could have appeared to influence the work reported in this paper.

## Data availability

Data will be made available on request.

## References

Amante, C., Eakins, B.W., 2009. Etopo1 1 Arc-Minute Global Relief Model: Procedures, Data Sources and Analysis. PANGAEA, NOAA-National Geophysical Data Center, NOAA technical memorandum. National Geophysical Data Center.

Apango-Figueroa, Ethel, Sánchez-Velasco, Laura, Lavín, Miguel F., Godínez, Victor M., Barton, Eric D., 2015. Larval fish habitats in a mesoscale dipole eddy in the Gulf of California. Deep. Sea Res. Part I: Ocean. Res. Pap. 103, 1–12.

Ardhuin, Fabrice, Chapron, Bertrand, Collard, Fabrice, 2009. Observation of swell dissipation across oceans. Geophys. Res. Lett. 36 (6).

Ardhuin, Fabrice, Gille, Sarah T., Menemenlis, Dimitris, Rocha, Cesar B., Rascle, Nicolas, Chapron, Bertrand, Gula, Jonathan, Molemaker, Jeroen, 2017. Small-scale open ocean currents have large effects on wind wave heights. J. Geophys. Res.: Ocean. 122 (6), 4500–4517.

Ardhuin, Fabrice, Rogers, Erick, Babanin, Alexander V., Filipot, Jean-François, Magne, Rudy, Roland, Aaron, van der Westhuysen, Andre, Queffeulou, Pierre, Lefevre, Jean-Michel, Aouf, Lotfi, Collard, Fabrice, 2010. Semiempirical dissipation source functions for ocean waves. Part I: Definition, calibration, and validation. J. Phys. Oceanogr. 40 (9), 1917–1941.

Ardhuin, Fabrice, Roland, Aron, Dumas, Franck, Bennis, Anne-Claire, Sentchev, Alexei, Forget, Philippe, Wolf, Judith, Girard, Françoise, Osuna, Pedro, Benoit, Michel, 2012. Numerical wave modeling in conditions with strong currents: Dissipation, refraction, and relative wind. J. Phys. Oceanogr. 42 (12), 2101–2120.

Arruda, Wilton Z., Silveira, I.C.A., 2019. Dipole-induced central water extrusions south of Abrolhos Bank (Brazil, 20.5°S). Cont. Shelf Res. 188, 103976.

Asiyabi, Reza Mohammadi, Ghorbanian, Arsalan, Tameh, Shaahin Nazarpour, Amani, Meisam, Jin, Shuanggen, Mohammadzadeh, Ali, 2023. Synthetic aperture radar (SAR) for ocean: A review. IEEE J. Sel. Top. Appl. Earth Obs. Remote. Sens. 16, 9106–9138.

Bao, M., Alpers, W., 1998. On the cross spectrum between individual-look synthetic aperture radar images of ocean waves. IEEE Trans. Geosci. Remote Sens. 36 (3), 922–932.

Beron-Vera, Francisco J., Olascoaga, Maria J., Goni, G.J., 2008. Oceanic mesoscale eddies as revealed by Lagrangian coherent structures. Geophys. Res. Lett. 35 (12).

Bôas, Ana B. Villas, Cornuelle, Bruce. D., Mazloff, Matthew. R., Gille, Sarah. T., Ardhuin, Fabrice, 2020. Wave–current interactions at meso- and submesoscales: Insights from idealized numerical simulations. J. Phys. Oceanogr. 50 (12), 3483–3500.

Brasil-Correa, Yuri O., Violante-Carvalho, Nelson, Santos, Felipe M., Carvalho, Luiz Mariano, Santos, Andre L.C., Costa, Leonardo P.F., Portilla-Yandun, Jesus, Romeiser, Roland, 2022. Evaluation of a linear inversion method for retrieval of directional wave spectra from SAR look cross spectra. Remote Sens. Environ. 282, 113265.

Calado, L., Gangopadhyay, A., Silveira, I.C.A., 2006. A parametric model for the Brazil Current meanders and eddies off southeastern Brazil. Geophys. Res. Lett. 33 (12), L12602.

Calado, L., Gangopadhyay, A., Silveira, I.C.A., 2008. Feature-oriented regional modeling and simulations (FORMS) for the western South Atlantic: Southeastern Brazil region. Ocean Modelling 25 (1–2), 48–64.

Chapron, B., Johnsen, H., Garello, R., 2001. Wave and wind retrieval from SAR images of the ocean. Ann. Des Télécommun. 56, 682–699.

Collard, F., Ardhuin, F., Chapron, B., 2009. Monitoring and analysis of ocean swell fields from space: New methods for routine observations. J. Geophys. Res.: Ocean. 114 (C7).

de Paula, Thiago Pires, Arruda, Wilton Zumpichiatti, Lima, Jose Antonio Moreira, Daher, Victor Bastos, Violante-Carvalho, Nelson, 2025. Spatial and temporal variability of the Brazil current path: Diagnostics from satellite-derived altimetry and a global reanalysis product. Deep. Sea Res. Part I: Ocean. Res. Pap. 219, 104474.

de Paula, Thiago Pires, Lima, Jose Antonio Moreira, Tanajura, Clemente Augusto Souza, Andrioni, Marcelo, Martins, Renato Parkinson, Arruda, Wilton Zumpichiatti, 2021. The impact of ocean data assimilation on the simulation of mesoscale eddies at São Paulo plateau (Brazil) using the regional ocean modeling system. Ocean. Model. 167, 101889.

dos Santos, Andre Luiz Cordeiro, dos Santos, Felipe Marques, Violante-Carvalho, Nelson, Carvalho, Luiz Mariano, Venceslau, Helder Manoel, 2025. The controlled four-parameter method for cross-assignment of directional wave systems. Ocean. Model. 197, 102584.

Dysthe, K.B., 2001. Refraction of gravity waves by weak current gradients. J. Fluid Mech. 442, 157–159.

Engen, G., Johnsen, H., 1995. SAR-ocean wave inversion using image cross spectra. IEEE Trans. Geosci. Remote Sens. 33 (4), 1047–1056.

Fedorov, K.N., Ginsburg, A.I., 1986. Mushroom-like currents (vortex dipoles) in the ocean and in a laboratory tank. In: Annales Geophysicae. Series B. Terrestrial and Planetary Physics, vol. 4, pp. 507–516.

Fedorov, K.N., Ginsburg, A.I., Kostianoy, A.G., 1989. Modelling of "mushroom-like" currents (vortex dipoles) in a laboratory tank with rotating homogeneous and stratified fluids. In: Elsevier Oceanography Series, vol. 50, Elsevier, pp. 15–24.

Goes, M., Cirano, M., Mata, M.M., Majumder, S., 2019. Long-term monitoring of the Brazil current transport at 22°S from XBT and altimetry data: Seasonal, interannual, and extreme variability. J. Geophys. Res.: Ocean. 124 (6), 3645–3663.

Hasselmann, S., Brüning, C., Hasselmann, K., Heimbach, P., 1996. An improved algorithm for the retrieval of ocean wave spectra from Synthetic Aperture Radar image spectra. J. Geophys. Res.: Ocean. 101 (C7), 16615–16629.

Hasselmann, K., Hasselmann, S., 1991. On the nonlinear mapping of an ocean wave spectrum into a Synthetic Aperture Radar image spectrum and its inversion. J. Geophys. Res.: Ocean. 96 (C6), 10713–10729.

Hersbach, Hans, Bell, Bill, Berrisford, Paul, Hirahara, Shoji, Horányi, András, Muñoz-Sabater, Joaquín, Nicolas, Julien, Peubey, Carole, Radu, Raluca, Schepers, Dinand, Simmons, Adrian, Soci, Cornel, Abdalla, Saleh, Abellan, Xavier, Balsamo, Gianpaolo, Bechtold, Peter, Biavati, Gionata, Bidlot, Jean, Bonavita, Massimo, De Chiara, Giovanna, Dahlgren, Per, Dee, Dick, Diamantakis, Michail, Dragani, Rossana, Flemming, Johannes, Forbes, Richard, Fuentes, Manuel, Geer, Alan, Haimberger, Leo, Healy, Sean, Hogan, Robin J., Hólm, Elías, Janisková, Marta, Keeley, Sarah, Laloyaux, Patrick, Lopez, Philippe, Lupu, Cristina, Radnoti, Gabor, de Rosnay, Patricia, Rozum, Iryna, Vamborg, Freja, Villaume, Sebastien, Thépaut, Jean-Noël, 2020. The ERA5 global reanalysis. Q. J. R. Meteorol. Soc. 146 (730), 1999–2049.

Johnsen, H., Engen, G., Collard, F., Chapron, B., 2006-10-24. Envisat ASAR Level 2 Wave Mode Product Algorithm Specification–Software Requirements Document. Technical Report IT650/1-01, NORUT.

Kenyon, Kern E., 1971. Wave refraction in ocean currents. Deep. Sea Res. Ocean. Abstr. 18 (10), 1023–1034.

Krogstad, H.E., Samset, O., Vachon, P.W., 1994. Generalizations of the non-linear ocean-SAR transform and a simplified SAR inversion algorithm. Atmos.-Ocean 32 (1), 61–82.

Lauton, Gustavo, Marta-Almeida, Martinho, Lentini, Carlos A.D., 2023. The effect of currents on large surface gravity waves under cyclonic conditions in the south/southeastern Brazil. J. Geophys. Res.: Ocean. 128 (3), e2022JC018472, e2022JC018472 2022JC018472.

Li, H., Stopa, J., Mouche, A., Zhang, B., He, Y., Chapron, B., 2021. Assessment of ocean wave spectrum using global Envisat/ASAR data and hindcast simulation. Remote Sens. Environ. 264, 112614.

Lucas, Cláudia, Guedes Soares, C., 2015. On the modelling of swell spectra. Ocean Eng. 108, 749–759.

Malan, Neil, Archer, Matthew, Roughan, Moninya, Cetina-Heredia, Paulina, Hemming, Michael, Rocha, Carlos, Schaeffer, Amandine, Suthers, Iain, Queiroz, Eduardo, 2020. Eddy-driven cross-shelf transport in the East Australian current separation zone. J. Geophys. Res.: Ocean. 125 (2), e2019JC015613.

Marechal, Gwendal, Ardhuin, Fabrice, 2021. Surface currents and significant wave height gradients: Matching numerical models and high-resolution altimeter wave heights in the agulhas current region. J. Geophys. Res.: Ocean. 126 (2), e2020JC016564, e2020JC016564 2020JC016564.

Massel, S.R., 2017. Ocean Surface Waves, third ed. World Scientific.

Mastenbroek, C., de Valk, C.F., 2000. A semiparametric algorithm to retrieve ocean wave spectra from Synthetic Aperture Radar. J. Geophys. Res.: Ocean. 105 (C2), 3497–3516.

Ni, Qinbiao, Zhai, Xiaoming, Wang, Guihua, Hughes, Chris W., 2020. Widespread mesoscale dipoles in the global ocean. J. Geophys. Res.: Ocean. 125 (10), e2020JC016479, e2020JC016479 2020JC016479.

Owda, Abdalmenem, Pleskachevsky, Andrey, Larsén, Xiaoli Guo, Badger, Merete, Cavar, Dalibor, Hasager, Charlotte Bay, 2024. Evaluation of SAR-based sea state parameters and roughness length derivation over the coastal seas of the USA. IEEE J. Sel. Top. Appl. Earth Obs. Remote. Sens. 17, 9415–9428.

Pereira, Henrique Patricio Prado, Violante-Carvalho, Nelson, Nogueira, Izabel Christina Martins, Babanin, Alexander, Liu, Qingxiang, de Pinho, Uggo Ferreira, Nascimento, Fabio, Parente, Carlos Eduardo, 2017. Wave observations from an array of directional buoys over the southern Brazilian coast. Ocean. Dyn. 67 (12), 1577–1591.

Portilla-Yandún, J., Valladares, C., Violante-Carvalho, N., 2019. A Hybrid Physical-Statistical Algorithm for SAR Wave Spectra Quality Assessment. IEEE J. Sel. Top. Appl. Earth Obs. Remote. Sens. 12 (10), 3943–3948.

Quilfen, Y., Yurovskaya, M., Chapron, B., Ardhuin, F., 2018. Storm waves focusing and steepening in the Agulhas current: Satellite observations and modeling. Remote Sens. Environ. 216, 561–571.

Rocha, Cesar B., Silveira, Ilson C.A., Castro, Belmiro M., Lima, Jose Antonio M., 2014. Vertical structure, energetics, and dynamics of the Brazil current system at 22°S–28° S. J. Geophys. Res.: Ocean. 119 (1), 52–69.

Romero, Leonel, Hypolite, Delphine, McWilliams, James C., 2020. Submesoscale current effects on surface waves. Ocean. Model. 153, 101662.

Romero, Leonel, Lenain, Luc, Melville, W. Kendall, 2017. Observations of surface wave–current interaction. J. Phys. Oceanogr. 47 (3), 615–632.

Santos, Felipe M., Santos, Andre L.C., Violante-Carvalho, Nelson, Carvalho, Luiz Mariano, Brasil-Correa, Yuri O., Portilla-Yandun, Jesus, Romeiser, Roland, 2021. A simulator of Synthetic Aperture Radar (SAR) image spectra: the applications on oceanswell waves. Int. J. Remote Sens. 42 (8), 2981–3001.

Schulz-Stellenfleth, J., Lehner, S., 2004. Measurement of 2-D sea surface elevation fields using complex synthetic aperture radar data. IEEE Trans. Geosci. Remote Sens. 42 (6), 1149–1160.

Schulz-Stellenfleth, J., Lehner, S., 2005. A noise model for estimated Synthetic Aperture Radar look cross spectra acquired over the ocean. IEEE Trans. Geosci. Remote Sens. 43 (7), 1443–1452.

Silveira, I.C.A., Pereira, Filipe, Flierl, Glenn R., Simoes-Sousa, Iury T., Palóczy, André, Borges-Silva, Milton, Rocha, César B., 2023. The Brazil current quasi-stationary unstable meanders at 22°S–23° S. Prog. Oceanogr. 210, 102925.

Vianello, Patrick, Ternon, Jean-François, Demarcq, Hervé, Herbette, Steven, Roberts, Michael J., 2020. Ocean currents and gradients of surface layer properties in the vicinity of the Madagascar Ridge (including seamounts) in the South West Indian Ocean. Deep. Sea Res. Part II: Top. Stud. Ocean. 176, 104816.

Violante-Carvalho, Nelson, Arruda, Wilton Z., Carvalho, Luiz Mariano, Rogers, W. Erick, Passaro, Marcello, 2021. Diffraction of irregular ocean waves measured by altimeter in the lee of islands. Remote Sens. Environ. 265, 112653.

Violante-Carvalho, Nelson, de Paula, Thiago, Calado, Leandro, dos Santos, Felipe Marques, Carvalho, Luiz Mariano, dos Santos, Andre Luiz Cordeiro, Arruda, Wilton Z., Farina, Leandro, 2025. Current effects on wind generated waves near an Ocean Eddy Dipole. Ocean. Model. 196, 102544.

Violante-Carvalho, N., Ocampo-Torres, F.J., Robinson, I.S., 2004. Buoy observations of the influence of swell on wind waves in the open ocean. Appl. Ocean Res. 26 (1), 49–60.

Violante-Carvalho, N., Robinson, I.S., 2004. Comparison of the two-dimensional directional wave spectra retrieved from spaceborne Synthetic Aperture Radar images using the MPI scheme against directional buoy measurements. Sci. Mar. 68 (3), 317–330.

Violante-Carvalho, N., Robinson, I.S., Gommenginger, C., Carvalho, L.M., Ocampo-Torres, F., 2012. The effect of the spatially inhomogeneous wind field on the wave spectra employing an ERS-2 SAR PRI image. Cont. Shelf Res. 36, 1–7.

Violante-Carvalho, N., Robinson, I.S., Schulz-Stellenfleth, J., 2005. Assessment of ERS Synthetic Aperture Radar wave spectra retrieved from the Max-Planck-Institut (MPI) scheme through intercomparisons of 1 year of directional buoy measurements. J. Geophys. Res.: Ocean. 110 (C7).

Wang, Jichao, Wang, Yue, 2022. Evaluation of the ERA5 significant wave height against NDBC Buoy Data from 1979 to 2019. Mar. Geod. 45 (2), 151–165.

WW3DG, 2019. User manual and system documentation of WAVEWATCH III version 6.07. NOAA/NWS/NCEP/MMAB. College Park, MD, USA, WAVEWATCH III Development Group, Tech. Note 326 pp.